Acta Pharmaceutica Sinica B 2022;12(10):3891−3904

Chinese Pharmaceutical Association
Institute of Materia Medica, Chinese Academy of Medical Sciences

Acta Pharmaceutica Sinica B

www.elsevier.com/locate/apsb
www.sciencedirect.com

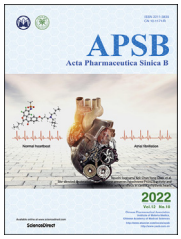

ORIGINAL ARTICLE

Development of a potential PET probe for HDAC6 imaging in Alzheimer's disease

Ping Bai[a], Prasenjit Mondal[b], Frederick A. Bagdasarian[a], Nisha Rani[a], Yan Liu[a], Ashley Gomm[b], Darcy R. Tocci[a], Se Hoon Choi[b], Hsiao-Ying Wey[a], Rudolph E. Tanzi[b], Can Zhang[b,*], Changning Wang[a,*]

[a]*Athinoula A. Martinos Center for Biomedical Imaging, Department of Radiology, Massachusetts General Hospital, Harvard Medical School, Charlestown, MA 02129, USA*
[b]*Genetics and Aging Research Unit, McCance Center for Brain Health, MassGeneral Institute for Neurodegenerative Disease, Department of Neurology, Massachusetts General Hospital, Harvard Medical School, Charlestown, MA 02129, USA*

Received 16 March 2022; received in revised form 18 April 2022; accepted 6 May 2022

KEY WORDS

HDAC6;
Alzheimer's disease;
Radiotracer;
PET imaging;
Epigenetic

Abstract Although the epigenetic regulatory protein histone deacetylase 6 (HDAC6) has been recently implicated in the etiology of Alzheimer's disease (AD), little is known about the role of HDAC6 in the etiopathogenesis of AD and whether HDAC6 can be a potential therapeutic target for AD. Here, we performed positron emission tomography (PET) imaging in combination with histopathological analysis to better understand the underlying pathomechanisms of HDAC6 in AD. We first developed [^{18}F]PB118 which was demonstrated as a valid HDAC6 radioligand with excellent brain penetration and high specificity to HDAC6. PET studies of [^{18}F]PB118 in 5xFAD mice showed significantly increased radioactivity in the brain compared to WT animals, with more pronounced changes identified in the cortex and hippocampus. The translatability of this radiotracer for AD in a potential human use was supported by additional studies, including similar uptake profiles in non-human primates, an increase of HDAC6 in AD-related human postmortem hippocampal tissues by Western blotting protein analysis, and our *ex vivo* histopathological analysis of HDAC6 in postmortem brain tissues of our animals. Collectively, our findings show that HDAC6 may lead to AD by mechanisms that tend to affect brain regions particularly susceptible to AD through an association with amyloid pathology.

*Corresponding authors. Tel.: +1 617 724 3983; fax: +1 617 726 7422.
E-mail addresses: Zhang.Can@mgh.harvard.edu (Can Zhang), cwang15@mgh.harvard.edu (Changning Wang).
Peer review under responsibility of Chinese Pharmaceutical Association and Institute of Materia Medica, Chinese Academy of Medical Sciences.

https://doi.org/10.1016/j.apsb.2022.05.017

1. Introduction

In the epigenetic mechanisms, histone deacetylases (HDACs) function as "erasers" that catalyze the removal of acetyl groups from acetylated histone, resulting in chromatin compaction and transcriptional repression[1]. There are 18 isotypes of HDACs identified in mammals, including Zn^{2+}-dependent HDACs (HDAC1−11) and NAD^{+}-dependent HDACs (known as sirtuins 1−7)[2]. The Zn^{2+}-dependent HDACs are further divided into three classes based on their size, cellular localization, and sequence homology to yeast HDAC deacetylases: class I (HDAC1−3 and 8), class II (HDAC4−7, 9 and 10), and class IV (HDAC11)[3]. Among these HDAC isoforms, HDAC6 is a unique enzyme that features two independent deacetylase domains (CD1 and CD2, presented at the N-terminal and the central region, respectively) and a C-terminal zinc finger domain for binding ubiquitinated proteins[4]. In addition, HDAC6 is primarily present in the cytosol and is the only HDAC able to deacetylate α-tubulin[4,5]. These features allow HDAC6 to regulate many diverse biological processes, including cell migration, cell proliferation and death, immune response, stress response, transcription, and degradation of misfolded proteins. It has been found that HDAC6 is closely associated with a variety of diseases. Many selective small-molecule HDAC6 inhibitors have been developed for the treatment of cancer and neurodegenerative diseases[6−8]. For example, ACY-241[9] and ACY-1215[10] are two selective HDAC6 inhibitors that have entered clinical trials for the treatment of multiple myeloma and other cancers. Notably, many recent reports have demonstrated the therapeutic potential of HDAC6 inhibitors in neurodegenerative diseases such as Alzheimer's disease (AD), Parkinson's disease (PD), and Huntington's disease (HD) in preclinical studies[11−15].

AD is currently one of the most common neurodegenerative disorders without effective treatment due to its complex etiologies. The link between HDAC6 and AD has attracted much attention in recent years. Several studies have found increased HDAC6 in the brain of AD patients, leading to decreased levels of acetylated α-tubulin, destabilized microtubules of neurons, and eventually causing neuronal dysfunction[15−17]. In addition, HDAC6 elevates the tau protein phosphorylation and results in the Aβ-induced neuropathological change[18,19]. Accordingly, HDAC6 is emerging as a novel therapeutic target for AD treatment. Several HDAC6 inhibitors have been used for AD treatment in preclinical studies[20]. Pharmacologic treatment of AD animal models with selective HDAC6 inhibitors exhibited therapeutical potential through improving axonal transport, reducing hyperphosphorylated tau protein, and inhibiting Aβ aggregation, thereby modulating AD pathogenesis[21−24]. Despite the cumulative evidence suggesting the links between HDAC6 and AD pathogenesis in preclinical models, the roles of HDAC6 in AD patients remain elusive. Understanding the expression and alteration of HDAC6 in the living brain will not only help to elucidate the pathological mechanisms of AD, but also advance the potential therapeutic development of targeting HDAC6 in AD.

Positron emission tomography (PET), an advanced molecular imaging technology, provides a non-invasive method to achieve a wealth of biological information in living subjects[25]. Imaging HDAC6 by PET may assess the physiological processes and quantify the expression level change of HDAC6 in AD, thereby enabling us to better understand the correlation between AD and HDAC6. In addition, PET imaging of HDAC6 may accelerate the discovery of new HDAC6 inhibitors for the treatment of central nervous system (CNS) disorders by measuring target engagement in the living brain. A number of HDAC6 radioligands have been reported for PET imaging in preclinical investigations[26]. However, most of the reported hydroxamic acid-based HDAC6 radioligands display poor brain penetration due to the high polarity of the hydroxamic acid moiety. Our group previously reported the first class I HDACs (HDAC1, 2, and 3) CNS PET radioligand, [^{11}C] martinostat, that has been approved for clinical studies[27] [^{11}C] Martinostat exhibits good brain uptake because the inclusion of an adamantyl group increased the lipophilicity for brain−blood barrier (BBB) penetration[28]. Based on this strategy, Strebl et al.[29−31] developed the HDAC6-selective radioligand [^{18}F]bavarostat (also known as [^{18}F]EKZ-001), which also exhibits good brain penetration. As the first HDAC6 PET probe capable of BBB penetrance, [^{18}F]bavarostat has been evaluated in preclinical studies of rodents and non-human primates and more recently completed its first-in-human studies[31]. However, the radiosynthesis of [^{18}F] bavarostat is not straightforward: there are three synthetic steps and one step requires a specific ruthenium complex for radiofluorination. As such, we focused our efforts on developing alternative CNS-penetrant radioligands that can be more readily synthesized for brain HDAC6 imaging.

In order to develop brain-permeable HDAC6 radioligands, we began with developing HDAC6 inhibitors with potent binding affinity, selectivity, and good brain penetration. Generally, the pharmacophore of selective HDAC6 inhibitors contains three domains: capping group, linker, and zinc-binding group[32]. Based on our previous experience in HDAC inhibitors and PET radioligands design, we found that the capping group plays a crucial role in the binding selectivity and brain permeability[27,33]. Inhibitors with large and rigid capping groups have a more suitable interaction with the wide hydrophobic cavity of the HDAC6 enzyme. Additionally, introducing the lipophilic capping group with fewer hydrogen-bond donors should help to enhance paracellular diffusion and increase BBB permeability. For example, Kozikowski and co-works[34] reported that a tetrahydroquinoline-based HDAC6 inhibitor, SW-100, exhibited good HDAC6 inhibitory activity, selectivity, and high brain uptake. After developing a series of potential brain-permeable HDAC6 inhibitors, we identified compound **15c**, termed PB118, as the most promising candidate for radioligand development [^{18}F]PB118 was thereby synthesized, and PET imaging studies were undertaken with [^{18}F] PB118 using both wild-type (WT) mice and 5xFAD AD transgenic mice. Particularly, these 5xFAD animals have been well-characterized which express familial AD (FAD) mutations in $APP^{Swedish/Florida/London}$ and $PS1^{M146L/L286V}$ and display classical amyloid neuropathology, especially in the cortex and hippocampus, however without showing evident tau pathology in the brain[35,36]. Supporting evidence of this radiotracer's potential for

clinical translation was confirmed with preliminary non-human primate PET imaging. Overall, our work is aimed to set the stage for further development of [^{18}F]PB118 as a useful HDAC6 imaging probe for AD and may facilitate the development of brain penetrant HDAC6 inhibitors as potential therapeutics of AD.

2. Results

2.1. Synthesis and biological evaluation of inhibitors *12a–i*

The preparation of HDAC6 inhibitors with different sizes of capping groups is straightforward with two synthetic steps (Scheme 1A). Several commercially available heterobicyclic secondary amines **2–10** were chosen as the starting materials to react with methyl 4-(bromomethyl)benzoate to afford the corresponding ester intermediates **11a–i**. The desired hydroxamate compounds **12a–i** were obtained by treating ester intermediates with aqueous NH_2OH/NaOH solution at room temperature for 1 h.

The inhibitory potency of compounds **12a–i** against HDAC1–11 was evaluated. Inhibitors with the benzo-fused *N*-heterobicyclic capping group (**12a–h**) exhibited good to moderate inhibitory activity and selectivity toward HDAC6 (Table 1). Among them, compound **12c** exhibited the most potent inhibitory activity and selectivity against HDAC6, with an IC_{50} of 11.8 nmol/L and a more than 100-fold selectivity for HDAC6 over other HDAC isoforms. The structure–activity relationship was further investigated based on the *in vitro* inhibition data. The position of the nitrogen atom on the capping group determined the steric configuration of the molecule, which played a critical role in HDAC6 inhibition. When the nitrogen was attached to the aromatic group (**12a** and **12c**), compounds showed low nanomolar HDAC6 potency (IC_{50} = 17.9 and 11.5 nmol/L, respectively) and over 100-fold greater selectivity for HDAC6. Additionally, the larger size of the capping group contributes to better HDAC6 inhibition. Generally, when the nitrogen atom presented in the same position, the HDAC6 inhibitory activity slightly increased with the capping group enlarging. For example, compared with the 6-membered ring compound **12a**, 7-membered ring compound **12c** exhibited enhanced HDAC6 inhibitory potency. The same trend was observed in compounds where the nitrogen atom is not attached to the aromatic group (**12d**, **12f**, and **12h**). Finally, replacing the aromatic group with aliphatic heterocycles (**12i**) resulted in reduced inhibition of HDAC6 and other HDAC isoforms, suggesting the pivotal role of benzo-fused capping group in HDAC6 inhibition.

2.2. Synthesis and biological evaluation of inhibitors *15a–d*

With compound **12c** poised as the most promising candidate for HDAC6 radioligand development, we then synthesized derivatives of **12c** with either a fluorine atom or methoxy group on the phenyl linker to explore potential radiolabeling strategies. The **12c** analogues bearing fluorine or methoxy group substituents (**15a–d**) were synthesized to evaluate HDAC6 potency and selectivity (Scheme 1B). As shown in Table 1, compared with **12c**, the analogue bearing a fluorine atom at the 3-C position of the phenyl linker (**15d**) exhibited slightly reduced HDAC6 potency (IC_{50} = 25.1 nmol/L) and comparable selectivity over the other 10 HDAC isoforms. Notably, compound **15c** (PB118), the analogue with a fluorine atom at the 2-C position of the phenyl linker, was found to have two-fold enhanced HDAC6 potency (IC_{50} = 5.2 nmol/L) and improved selectivity (>119-fold over other HDAC isoforms) compared to **12c**. On the other hand, the introduction of the methoxy group on the phenyl linker (**15a** and **15b**) resulted in dramatically reduced HDAC potency. In light of the favorable HDAC6 binding affinity and selectivity exhibited by PB118, we screened the off-target profile of PB118 using radioligand assays by the National Institute on Mental Health-Psychoactive Drug Screening Program (PDSP). No significant off-target binding was observed in a panel of 46 CNS targets at a 10 μmol/L concentration of PB118 (Supporting Information Table S1). Based on the *in vitro* biological evaluation, we selected PB118 as our HDAC6 PET radioligand candidate for further exploration.

2.3. Molecular modeling and stimulation of PB118

Molecular docking was carried out to better understand the ligand–protein interaction of PB118 with HDAC6. PB118 was docked into an available zHDAC6 crystal structure (PDB entry 6THV) with AutoDock Vina[37,38]. As shown in Fig. 1C, the hydroxamate group of PB118 presents adjacent to the zinc ion and

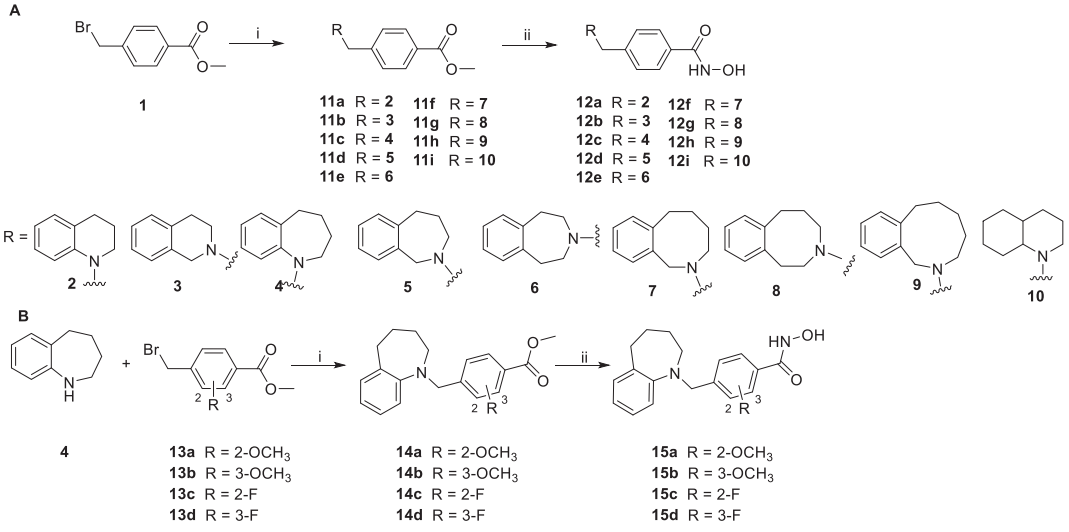

Scheme 1 Synthesis of *N*-heterobicyclic HDAC6 inhibitors. Reagents and conditions: (i) K_2CO_3, acetone, reflux, 6–8 h; (ii) NaOH, 50% (*w*/*w*) aq. NH_2OH, THF/MeOH (1:1), 0 °C to rt, rt, 1 h.

Table 1 Full of 11 HDAC isoforms profiling of synthetic compounds[a].

Compd.	IC_{50} (nmol/L)										
	HDAC isoforms										
	1	2	3	4	5	6	7	8	9	10	11
12a	3090	7060	1805	7990	>10,000	17.9	>10,000	7060	>10,000	>10,000	>10,000
12b	>10,000	>10,000	7720	>10,000	>10,000	307	>10,000	7060	>10,000	>10,000	>10,000
12c	2490	6840	1296	3870	>10,000	11.5	2500	2900	>10,000	4840	3790
12d	>10,000	>10,000	>10,000	>10,000	>10,000	251	>10,000	>10,000	>10,000	>10,000	>10,000
12e	6950	>10,000	3570	8000	>10,000	396	9490	5440	9710	>10,000	>10,000
12f	8470	>10,000	3040	3480	>10,000	213	3030	2730	2770	>10,000	>10,000
12g	>10,000	>10,000	3710	7050	>10,000	178	5150	4350	6120	>10,000	>10,000
12h	2570	>10,000	852	3720	>10,000	103	307	2680	3860	4080	>10,000
12i	>10,000	>10,000	7230	7990	>10,000	453	3160	6470	7630	>10,000	>10,000
15a	>10,000	>10,000	>10,000	>10,000	>10,000	6456	>10,000	>10,000	>10,000	>10,000	9520
15b	>10,000	>10,000	>10,000	>10,000	>10,000	4160	>1000	2060	>10,000	>10,000	3520
15c (PB118)	7820	>10,000	2960	2120	2440	5.2	609	1680	3150	8960	4380
15d	>10,000	>10,000	2460	3560	>10,000	25.1	3020	9110	>10,000	>10,000	5420
TSA	1.1	3.2	0.3	1210	1380	2.07	445	242	5370	1.48	9080

[a]IC_{50} values are the mean of two experiments obtained from curve-fitting of a 12-point enzymatic assay starting from 10 μmol/L with 3-fold serial dilution against all 11 HDAC isoforms; Trichostatin A (TSA) was used as a positive control.

engages in the monodentate interaction. Two hydrogen bonds between the NH of the hydroxamate group and Phe583 as well as OH and His574 are formed, which results in the reinforced binding potency. The $\pi-\pi$ stacking interactions between the rigid phenyl linker of PB118 and Phe583 and Phe643 are formed in the hydrophobic channel of HDAC6. The surface pose of PB118 (Fig. 1D) in the HDAC6 indicates that the hydroxamate group entered the catalytic pocket deeply, and the fluorophenyl linker occupies the hydrophobic channel appropriately. Notably, the presence of fluorine atom on the phenyl ring does not affect the HDAC6 binding affinity and contributes to favorable van der Waals interactions by pointing to the residues of Phe643 and Leu 712 in the so-called L1-loop pocket. The large and rigid capping group, tetrahydrobenzazepine, presents on the surface of the L1-loop pocket and forms water-mediated interactions with residues of Pro464, Tyr745, and His463. The favorable position of tetrahydrobenzazepine capping group enables PB118 to fit HDAC6 and improves its selectivity profile.

2.4. *Physicochemical properties of PB118*

The lipophilicity of PB118 through the "shake flask method" and determined its log$D_{7.4}$ value of 3.4, which is within the favorable range of CNS PET radioligand (log$D_{7.4}$ < 3.5). The topological polar surface area of PB118 was predicted by ChemBioDraw Ultra 16.0 (Table 2), which, combined with the lipophilicity study, demonstrates the appropriate physicochemical properties of PB118.

2.5. *In vitro ADME evaluation and in vivo brain/plasma pharmacokinetic profiling of PB118*

To evaluate the radioligand-like as well as drug-like properties of PB118, we further carried out the *in vitro* ADME assessments and *in vivo* brain/plasma pharmacokinetic studies. As shown in Table 2, PB118 exhibited good metabolic stability in human liver microsomal fraction and hepatocyte, with half-lives ($t_{1/2}$) of 67.9 min and 32.4 min, respectively. Moreover, no significant

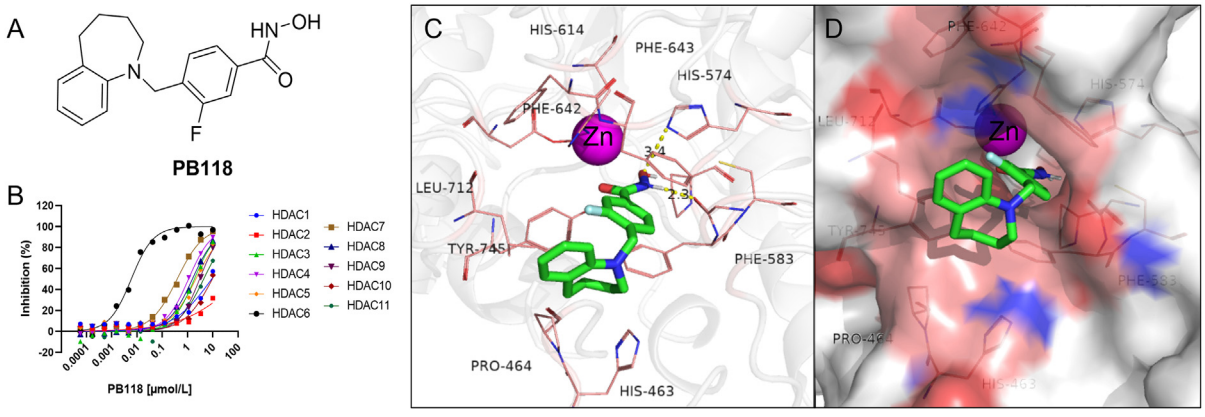

Figure 1 Molecular Modeling and Stimulation of PB118. (A) Chemical structure of PB118 and (B) its inhibitory activities against HDAC1−11. (C) Molecular docking study results of PB118 based on the zHDAC6 crystal complex (PDB entry 6THV). Zn ion is shown as a purple sphere and hydrogen bonds as yellow dotted lines; key amino acid residues that create the specific pocket in HDAC6 are represented as a stick and labeled as shown. (D) Surface poses of PB118 in the HDAC6 binding pocket.

Table 2 ADME/PK studies of PB118[a].

Property			
Physicochemical property			
MW	314.3	Log$D_{7.4}$	3.4
tPSA	52.57	*c*Log*P*	3.76
IC_{50} for HDAC6 (nmol/L)	5.2	SI	>117
In vitro **ADMET profile**			
Liver microsomal stability ($t_{1/2}$, min)		Human	67.9
Hepatocyte stability ($t_{1/2}$, min)		Human	32.4
CYP inhibition (% @10 μmol/L)		1A2	36.8
		2C9	34.8
		2C19	54
		2D6	36.3
		3A4T	89
Plasma protein binding (%)		Human	99.40%
In vivo **brain/plasma PK studies (ip, 1 mg/kg)**			
Time (h)	0.5	1	4
Brain con. (ng/mL)	48.5	11.5	0.82
Plasma con. (ng/mL)	1.32	0.72	0.35
Brain/plasma ratio	37	0.35	2.3

[a]*c*Log*P* and tPSA are calculated by ChemBioDraw Ultra 16.0. SI means HDAC6 selectivity index over other HDAC isoforms. ADME studies and *in vivo* PK profiling were conducted by HD Biosciences (China) Co., Ltd. For brain/plasma PK studies, C57BL/6 male mice were treated with PB118 by ip administration at the dose of 1 mg/kg. Blood and brain samples were collected at 0.5, 1, and 4 h time points. The plasma and brain samples were processed using acetonitrile precipitation and analyzed by LC−MS/MS. Data are expressed as the mean of three repeat experiments.

inhibition of cytochrome P450 enzymes (CYPs) 1A2, 2C9, 2C19, and 2D6 by PB118 was observed. Additionally, PB118 showed a human plasma protein rate of 99.4%, which is generally in an acceptable range. The *in vivo* brain/plasma PK studies were performed by IP administrating PB118 at 1 mg/kg in C57BL/6 mice. PB118 exhibited a high brain/plasma ratio of 37 at 30 min, 16 at 1 h, and 2.3 at 4 h postinjection.

2.6. *Radiochemistry*

The radiosynthesis of [^{18}F]PB118 was achieved via a two-step reaction (Scheme 2): (1) the arylboronic ester precursor **16** was reacted with K_{222}/[^{18}F]KF in the presence of $Cu_2(OTf)_2$ $(py)_4$ in DMA at 120 °C for 20 min to afford [^{18}F]**14c**; (2) [^{18}F]PB118 was obtained by treating [^{18}F]**14c** with aqueous NH_2OH/NaOH solution at room temperature for 10 min. As a result [^{18}F]PB118 was prepared in 120 min, with an average radiochemical yield (RCY) of 10% (n = 6, decay corrected), over 95% radiochemical purity, and over 110 GBq/μmol molar activity.

2.7. *PET imaging of WT mice with [^{18}F]PB118*

With the radioligand available, we first performed dynamic PET scans with [^{18}F]PB118 in rodents. Male C57BL/6 mice (n = 4) were administrated with [^{18}F]PB118 (tail intravenous injection) before 60 min PET acquisition and 10 min computed tomography (CT) scan. The summed PET/CT images (0−60 min) and time−activity curves (TACs) in the whole brain of mice were generated to assess the BBB permeability of [^{18}F]PB118 *in vivo*. As shown in Fig. 2A [^{18}F]PB118 exhibited an excellent brain

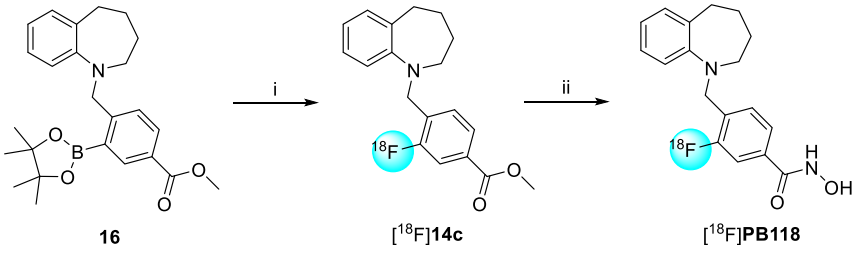

Scheme 2 Radiosynthesis of [^{18}F]PB118. Reagents and conditions: (i) K_{222}/[^{18}F]KF, $Cu_2(OTf)_2$ $(py)_4$, DMA, 120 °C, 20 min. RCY: 14%−16% (non-decay-corrected, n = 6); (ii) 0.6 mol/L NaOH, NH_2OH (50% (*w*/*w*) in H_2O), MeOH/THF (1:1), 10 min. RCY: 66%−70% (non-decay-corrected). Molar activity: 110 GBq/μmol (EOB).

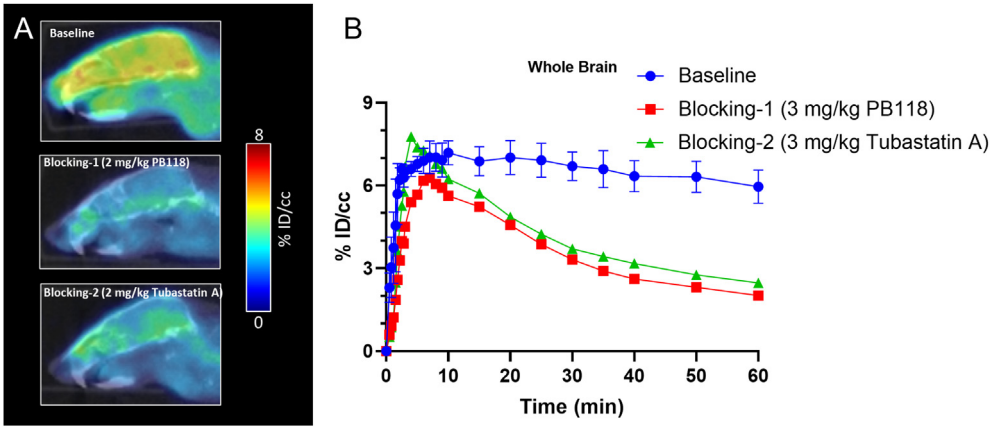

Figure 2 PET imaging studies of [^{18}F]PB118 in WT mice. (A) Representative PET images of [^{18}F]PB118 focus on the mice brain (0−60 min; midbrain axial); (B) the baseline and blocking (2.0 mg/kg unlabeled PB118 and 2.0 mg/kg HDAC6 selective inhibitor tubastatin A) time−activity curves of [^{18}F]PB118 in the mice whole brain (n = 4). The data were expressed as mean ± SD, n = 4.

uptake with the maximum percent injection dose per cubic centimeter (% ID/cc) of 7, which is well above the CNS radiotracers' minimum brain uptake requirement (% ID/cc > 0.1). TAC analysis indicated that [^{18}F]PB118 had a fast brain penetration in the first few minutes post-injection and bonded to HDAC6 over the 60 min PET acquisition suggesting the suitable kinetic profile of [^{18}F]PB118.

To evaluate the specific binding of [^{18}F]PB118, homologous and heterologous blocking studies were carried out by pretreating unlabeled PB118 and known selective HDAC6 inhibitor Tubastatin A 5 min prior to tracer injection. According to the TAC of mice pretreated with blocking agent [^{18}F]PB118 penetrated the brain and washout rapidly without binding to HDAC6 due to the target pre-occupancy. Compared with baseline mice, remarkably reduced radioactivity was observed in the brain of blocking mice (Fig. 2B).

2.8. *PET imaging of AD mice with [^{18}F]PB118*

The promising performance of [^{18}F]PB118 in PET imaging studies in mice encouraged us to apply it to investigate HDAC6 in an AD model. Further PET imaging with [^{18}F]PB118 was

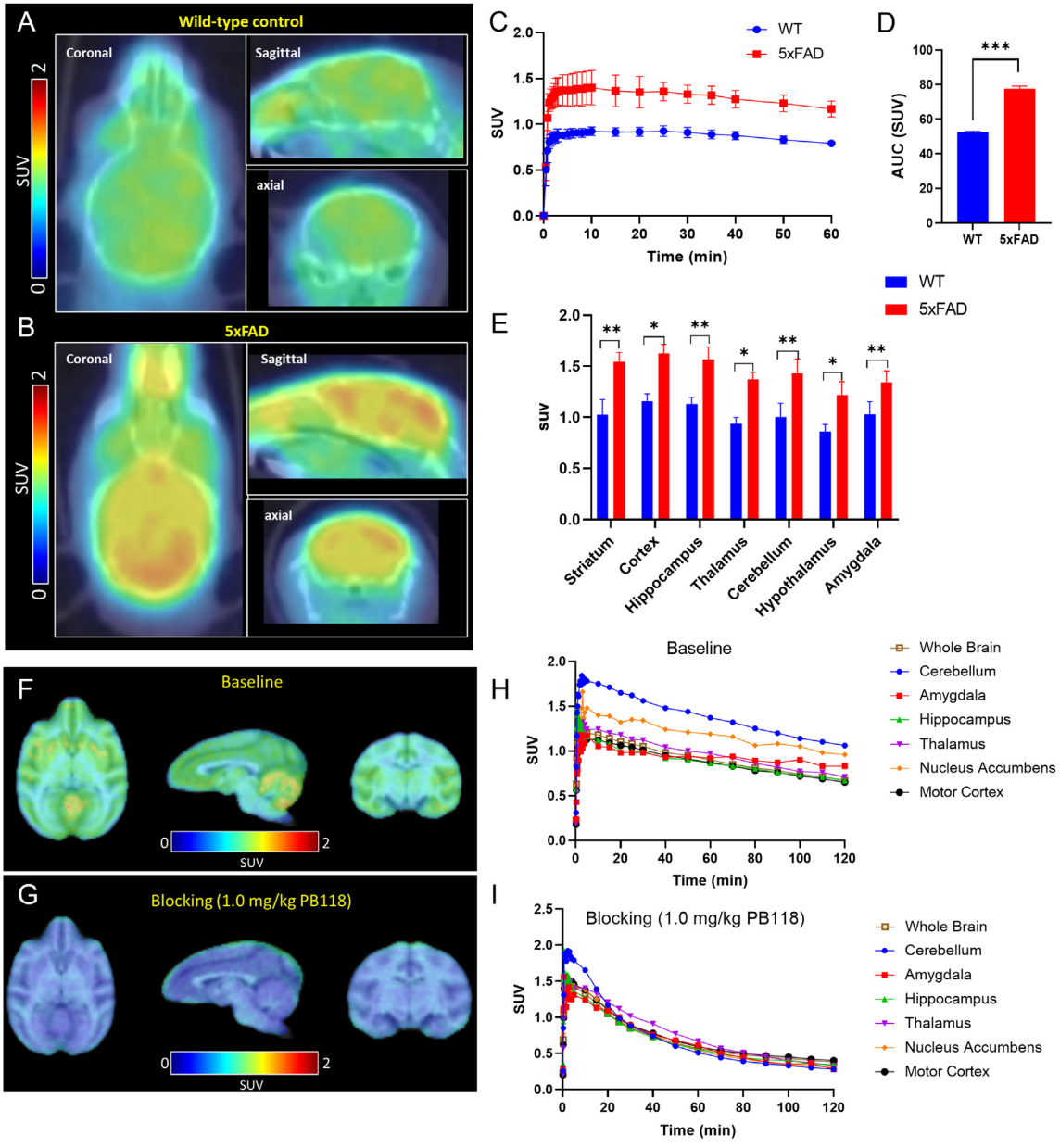

Figure 3 PET imaging studies of [^{18}F]PB118. (A) Representative summed PET/CT images (0−60 min, show as sagittal slices, coronal slices, and midbrain axial) focus on the brain of WT mice and (B) 5xFAD mice. (C) TACs of [^{18}F]PB118 in the whole brain of WT and 5xFAD mice. (D) the area under the curve (AUC) of TACs in (C) shows a statistically significant difference in [^{18}F]PB118 brain uptake in WT and 5xFAD mice. (E) Regional brain biodistribution of [^{18}F]PB118 in cortex, cerebellum, thalamus, hypothalamus, striatum, hippocampus, and amygdala in WT and 5xFAD mice. (F)−(G) Representative PET/MR baseline and blocking SUV images of a rhesus monkey brain, averaged from 90 to 120 min, after intravenous injection of [^{18}F]PB118. (H)−(I) TACs of [^{18}F]PB118 in the regions of interest in baseline and blocking studies. All data are expressed as mean ± SD, $n = 4$; Asterisks indicate statistical significance. *$P < 0.05$, **$P \leq 0.01$, and ***$P \leq 0.001$.

conducted in 6-month-old male 5xFAD transgenic mice model of AD and their respective age-matched wild-type (WT) strains ($n = 4$ for each group). PET results indicated a higher radioactivity signal in the brain was detected in 5xFAD mice relative to age-matched WT mice (Fig. 3A and B). The uptake of [^{18}F]PB118 in the mice brain was expressed as standard uptake value (SUV) for analysis, and the TACs were shown in Fig. 3C. Although there was a similar shape of TACs in WT and 5xFAD mice brains, a statistically significant increase in [^{18}F]PB118 uptake in the 5xFAD mice was found, which indicates the higher expression of HDAC6 in AD. To investigate the regional brain biodistribution of HDAC6 in WT and 5xFAD animals, we carried out the analysis of [^{18}F]PB118 uptake in different brain regions of these animals. Seven regions of interest (ROIs), including striatum, cortex, hippocampus, thalamus, cerebellum, hypothalamus, and amygdala, were selected according to the FUSION module (Ma-Benveniste-Mirrione, a mice brain regional analysis module) in PMOD (PMOD 4.003, PMOD Technologies Ltd., Zurich, Switzerland). Heterologous distribution of radioactivity was observed in the ROIs in WT and 5xFAD mice. As the histogram depicted in Fig. 3E, [^{18}F]PB118 had a similar biodistribution in the ROIs in WT and 5xFAD, with the high radioactivity level observed in the regions of cortex, hippocampus, and striatum, while the relative low radioactivity found in thalamus and hypothalamus. Similar to the whole brain analysis, 5xFAD mice exhibited increased radioactivity uptake in each ROI, especially in the regions of the hippocampus, striatum, and amygdala that are correlated with learning, memory, and cognition.

2.9. *Non-human primate (NHP) PET/MR imaging of [^{18}F] PB118*

Dynamic PET/MR scans after administration of [^{18}F]PB118 were carried out in two male rhesus macaques (weight = 9 and 12.3 kg, respectively) for a baseline and a self-blocking scan. As the images and TACs generated in Fig. 3H [^{18}F]PB118 exhibited good brain penetration with a peak SUV of 1.3 in the whole brain under baseline condition. Heterogeneous distribution of the radioactivity was also observed throughout the segmented brain regions. The cerebellum exhibited the highest radioactivity uptake, followed by the nucleus accumbens, thalamus, and hippocampus (Fig. 3H). In the blocking study, pretreating with 1.0 mg/kg unlabeled PB118 immensely decreased the radioactivity uptake compared to the baseline measurements (Fig. 3F and G). The TACs (Fig. 3I) indicate that [^{18}F]PB118 uptake was inhibited in all regions of interest evaluated and the tracer washed out from the brain rapidly.

2.10. *Ex vivo studies of HDAC6 expression change in AD brain*

To further analyze HDAC6 changes in AD, we next performed Western blot (WB) assay in human health and AD brain tissues as well as immunofluorescence microscopy-based IHC staining of HDAC6 in WT and 5xFAD animal brain sections. The WB analysis showed that the expression level of HDAC6 significantly increased in AD patients' hippocampus relative to healthy control (Fig. 4A and B). We also characterized the expression and distribution of HDAC6 in 3-month old male WT (Fig. 4C) and 5xFAD transgenic (Fig. 4D) animals. We found an increase of HDAC6 signal in overall brain areas comparing 5xFAD to WT animals, including the cortex and hippocampus, consistent with our PET imaging results.

To better characterize HDAC6 expression, we further co-stained with the well-characterized GFAP antibody to show astrocytes (green), as well as the Hoechst dye to show nuclei (blue). Our images were taken in 4 × (Fig. 5A and C) and 40 × (Fig. 5B and D) confocal objectives (Nikon C2). The white box in Fig. 5A and C in the hippocampal CA3 region was further analyzed in higher magnification in Fig. 5B and D, respectively. Scale bars correspond to 100 μm (Fig. 5A and C) and 10 μm (Fig. 5B and D). Notably, HDAC6 expression was primarily characterized by cytoplasmic distribution across different brain areas with minor aggregation-like perinucleus distribution in the brain of these 3-month animals (Fig. 5). Our results warrant further studies in older animals for potential age-dependent HDAC6 changes in AD. Additionally, we performed higher magnification images in other brain areas (Supporting Informaiton Fig. S2) that were previously shown with significant changes in these animals. These areas included the cortex and hippocampal dentate gyrus of WT animals (Fig. S2A, C and E) and 5xFAD animals (Fig. S2B, D and F). Furthermore, our quantifications of HDAC6 intensity showed that HDAC6 signal was significantly higher in the hippocampus (Fig. 5E) and cortex (Fig. 5F) in 5xFAD animals than those in WT animals, respectively ($^{*}P < 0.05$), which was accordant with our PET imaging results. Thus, our biochemical results of postmortem brain tissues are consistent with our PET findings for HDAC6 expression and suggest HDAC6 is a protein that is early responsive to amyloid pathology of AD.

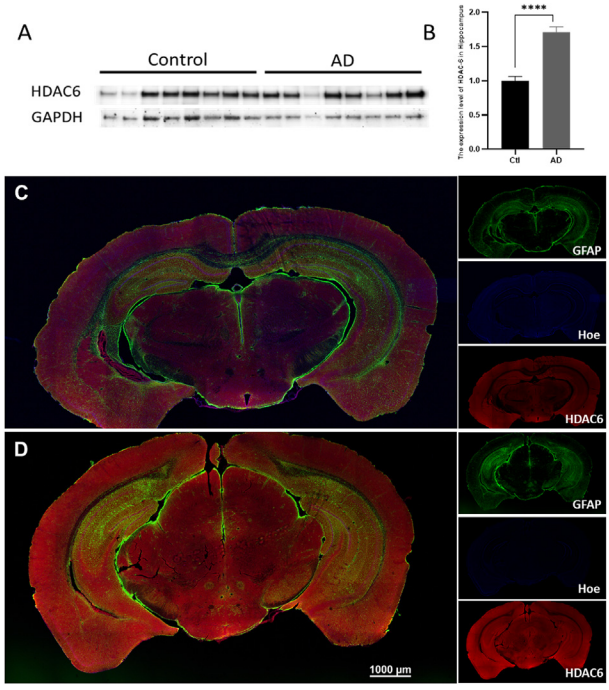

Figure 4 *In vitro* studies of HDAC6 expression change in AD brain. (A) Representative results of Western blot analysis displayed the levels of HDAC6 in human AD brain hippocampal tissues. (B) Quantification HDAC6 were normalized to the levels of GAPDH. $^{****}P < 0.0001$, Ctl *vs.* AD. (C) and (D) Immunofluorescence microscopy-based IHC staining images for HDAC6. Imaging of brain sections of animals, including WT (C) and 5xFAD (D) were shown using the HDAC6 antibody for HDAC6 (red), which was co-stained with the GFAP antibody for astrocytes (green) and Hoechst for nuclei (blue). Ctl, control; Hoe, Hoechst.

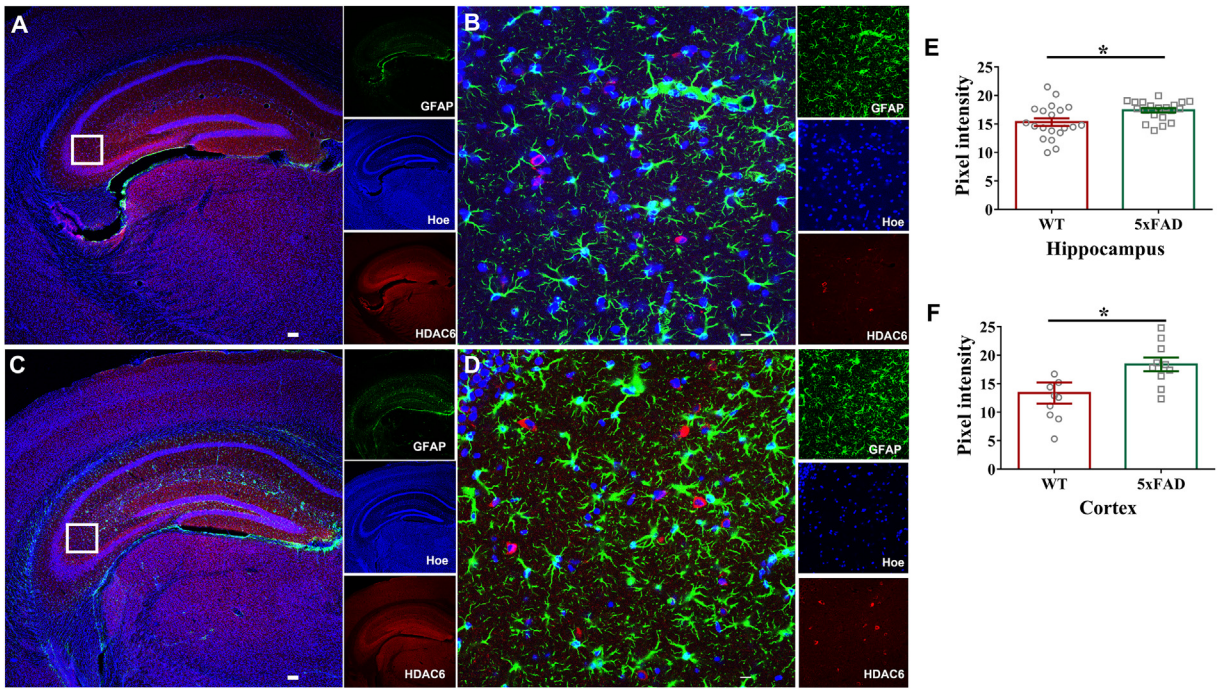

Figure 5 Immunofluorescence microscopy-based IHC staining of HDAC6 in WT and 5xFAD animal brain sections. HDAC6 expression was analyzed by IHC on the coronal brain sections in WT (A and B) animals ($n = 3$) and 5xFAD (C and D) animals ($n = 3$) using the HDAC6 antibody for HDAC6 (red), in addition to the GFAP antibody for astrocytes (green), and Hoechst for nuclei (blue). Images were taken in 4 × (A, C) and 40 × (B, D) confocal objectives (Nikon C2). White box in A and C in the hippocampal CA3 region were further analyzed in higher magnification in B and D, respectively. Scale bars correspond to 100 μm (A, C) and 10 μm (B, D). HDAC6 intensity in the hippocampus (E) and cortex (F) was quantified comparing WT and 5xFAD animals, respectively. Data are mean ± SEM; two-tailed unpaired *t*-test; $^*P < 0.05$.

3. Discussion

In this study, we showed that HDAC6 is a critical player in AD using transgenic animals expressing amyloid neuropathology in their brains. Despite considerable evidence showing HDAC6 in association with the tau protein, we provided evidence strongly suggesting that HDAC6 plays critical roles in the amyloid pathology of AD and that HDAC6 can provide a suitable target enabling inhibition-based drug development of AD. Specifically, we developed a new PET imaging probe which was successfully validated and subsequently utilized in living AD transgenic animals in combination with our *ex vivo* histopathological analysis of human and animal brains, both of which showed increased HDAC6 in AD.

Regarding our molecular imaging-based studies, to develop a brain penetrant PET probe for HDAC6 imaging, we first designed and synthesized a series of HDAC6 inhibitors utilizing the larger benzo-fused *N*-heterobicyclic as the capping group to increase the target selectivity and brain uptake. In addition, our previous work has identified that fluorination of aromatic ring on phenyl linker could improve the binding selectivity for HDAC6, metabolic stability while facilitating radiolabeling with fluorine-18[39]. Following this strategy, after the pharmacological screening of designed compounds, PB118 was identified as the most potent HDAC6 inhibitor with good binding affinity and selectivity. Further characterizations of PB118 were carried out to predict the *in vivo* properties as a PET ligand. The favorable physicochemical, pharmacological, kinetic, and metabolic performance of PB118 prompted us to radiolabel it with fluorine-18 and conduct PET imaging in animals for further investigation. In previous studies, despite considerable evidence showing HDAC6 as a tau-interacting protein, it is not well-characterized for HDAC6 in association with amyloid neuropathology, and little is known the exact role of HDAC6 plays in the etiopathogenesis of AD, nor HDAC6 changes in the brain areas of AD. Thus, we chose 5xFAD mice as the animal model for the PET imaging studies to investigate these unresolved questions. 5xFAD mice are AD transgenic animals that express familial AD (FAD) mutations in $APP^{Swedish/Florida/London}$ and $PS1^{M146L/L286V}$ and display classical amyloid neuropathology, especially in the cortex and hippocampus, however without showing evident tau pathology in the brain. In our subsequent PET studies of [^{18}F]PB118, 5xFAD mice showed the heterologous distribution of radioactivity in brain regions and significantly increased radioactivity uptake compared to the WT mice. These observations are consistent with the previous *in vitro* studies results and published reports, suggesting a strong link between elevations in HDAC6 and AD through non-invasive PET imaging in living subjects[40–42]. Following, radioactivity uptake profiles and preferable washout in NHP further support the utility of this novel radioligand in higher mammalian species. The successful inhibition of uptake through pre-treatment with non-radiolabeled PB118 indicates high specific binding in the primate brain. These features indicate that [^{18}F]PB118 has more favorable tracer properties than existing HDAC6 probes such as [^{18}F]Bavarostat[30]. For example, compared with [^{18}F]Bavarostat [^{18}F]PB118 has better binding affinity and selectivity for HDAC6 (binding affinity: $IC_{50} = 5.2$ *vs.* 60 nmol/L, selectivity: >119-fold *vs.* >78-fold over other HDACs), corresponding to a higher specific binding than [^{18}F]Bavarostat. Besides [^{18}F]PB118 showed more suitable kinetics in NHP studies than [^{18}F]Bavarostat, which

may contribute to kinetic modeling in future studies. Our future studies will characterize the tracer kinetic properties of [^{18}F]PB118 and quantify [^{18}F]PB118 availability by incorporating arterial plasma and radio-metabolites data with pharmacokinetic modeling methods to elucidate [^{18}F]PB118 cerebral volumes of distribution.

Our PET molecular imaging of HDAC6 was based on small molecule-based probe specific for HDAC6 in live animals. In previous studies, immunofluorescence analysis of HDAC6 was performed to detect its expression in cells and postmortem human brain tissues. The results showed that HDAC6 is primarily characterized by cytoplasmic localization in cultured cells and human brain sections[17]. Furthermore, the distribution of HDAC6 showed largely homogeneous properties in normal conditions and displayed aggregation-like perinucleus and nucleus expression patterns under stress[17]. A previous study showed that ApoE 4 transgenic mice might lead to increased HDAC6 nucleus expression in the hippocampus compared to ApoE 3 transgenic mice or wild-type controls[43]. Thus, we characterized HDAC6 using WB assay in human brain hippocampal tissues and immunofluorescence-based immunohistochemistry in postmortem brain tissues of animals. The *in vitro* WB and immunofluorescence assays showed significantly increased HDAC6 expression in AD, consistent with our PET imaging results. Notably, our results also support an amyloid pathology-related HDAC6 increase which is independent of tau pathology in AD. Collectively, our findings, in combination with previous reports, support an increase of HDAC6 in AD and suggest HDAC6 inhibitors as potential therapeutics for AD.

4. Conclusions

In order to develop a brain penetrant PET probe for HDAC6 imaging, we designed and synthesized a series of benzo-fused *N*-heterobicyclic derivatives as the potential brain-permeable HDAC6 inhibitors. Pharmacological evaluation of these derivatives demonstrated that compound PB118 has excellent HDAC6 binding affinity and selectivity. Further characterizations of PB118 showed good metabolic stability and favorable brain permeability [^{18}F]PB118 was successfully prepared with a resealable RCY and high molar activity. PET imaging of [^{18}F]PB118 was then performed in rodents. As expected [^{18}F]PB118 showed high brain uptake and good specific binding in mice and NHP. Furthermore, PET studies of [^{18}F]PB118 in 5xFAD mice showed the heterologous distribution of radioactivity in brain regions and significantly increased radioactivity uptake in 5xFAD mice compared to the WT mice, consistent with the *in vitro* immunofluorescence assay. Our results support an increase of HDAC6 in AD and suggest HDAC6 inhibitors as potential therapeutics for AD. In summary, PB118 shows great promise as a potential therapeutic agent against AD and as a PET probe for HDAC6 imaging in AD in preclinical studies, which warrants further development enabling investigations in the clinic.

5. Experimental

All commercially available chemical reagents and solvents were ordered from commercial suppliers in ACS-grade purity or higher, and directly used without further purification. Tubastatin A was purchased from MedChemExpress. NMR spectra were collected in a JEOL NMR-ECZ500R Spectrometer at room temperature (500 MHz (^{1}H), 471 MHz (^{19}F), and 126 MHz (^{13}C)). Chemical shifts were given in δ values (ppm), using tetramethylsilane (TMS) as the internal standard. Mass spectrometry data were recorded on an Agilent 6310 ion trap mass spectrometer (ESI source) connected to an Agilent 1200 series HPLC with a quaternary pump, vacuum degasser, diode-array detector, and autosampler.

All animal studies were carried out at Massachusetts General Hospital (PHS Assurance of Compliance No. A3596-01, USA). The Subcommittee on Research Animal Care (SRAC) serves as the Institutional Animal Care and Use Committee (IACUC) for the Massachusetts General Hospital (MGH). SRAC reviewed and approved all procedures detailed in this paper.

No-carrier-added ^{18}F-fluoride was produced from water 97% enriched in ^{18}O (Sigma−Aldrich®) by the nuclear reaction ^{18}O (p, n)^{18}F with a Siemens Eclipse HP cyclotron and a silver-bodied target at Athinoula A. Martinos Center for Biomedical Imaging. The produced ^{18}F-fluoride in water was transferred from the cyclotron target by helium push.

5.1. General procedure for synthesis of intermediates **11a−i** and **14a−d**

To a stirred mixture of **1** methyl 4-(bromomethyl)benzoate (100 mg, 0.44 mmol) and K_2CO_3 (72.4 mg, 0.52 mmol) in acetone (10 mL) was added the corresponding heterobicyclic secondary amines **2−10** (0.44 mmol). The resulting mixture was stirred at 60 °C for 6−8 h. After the completion of reaction, the acetone was evaporated under reduced pressure and the residue was purified by silica gel chromatography to afford the desired products.

Methyl 4-((3,4-dihydroquinolin-1(2H)-yl)methyl)benzoate (***11a***). Light yellow solid; Yield: 77.1%. ^{1}H NMR (500 MHz, chloroform-*d*) δ 7.68 (d, J = 8.0 Hz, 2H), 7.35 (d, J = 7.9 Hz, 2H), 7.14 (td, J = 7.1, 2.0 Hz, 1H), 7.09−7.04 (m, 1H), 7.02 (td, J = 7.5, 1.8 Hz, 2H), 3.91 (s, 3H), 3.86 (s, 2H), 2.90 (t, J = 6.3 Hz, 2H), 2.46−2.44 (m, 2H). MS (ESI+): 282.2 [M + H]$^+$.

Methyl 4-((3,4-dihydroisoquinolin-2(1H)-yl)methyl)benzoate (***11b***). Light yellow solid; Yield: 70.6%; ^{1}H NMR (500 MHz, chloroform-*d*) δ 7.66 (d, J = 8.0 Hz, 2H), 7.37 (d, J = 7.9 Hz, 2H), 7.25 (t, J = 7.1 Hz, 1H), 7.09−7.04 (m, 1H), 7.02 (td, J = 7.5, 1.8 Hz, 2H), 3.81 (s, 3H), 3.66 (s, 2H), 2.92−2.88 (m, 2H), 2.45−2.41 (m, 2H). MS (ESI+): 282.2 [M + H]$^+$.

Methyl 4-((2,3,4,5-tetrahydro-1H-benzo[b]azepin-1-yl)methyl) benzoate (***11c***). Light yellow solid; Yield: 73.2.^{1}H NMR (500 MHz, chloroform-*d*) δ 8.01 (d, J = 8.2 Hz, 2H), 7.51 (d, J = 8.1 Hz, 2H), 7.16−7.10 (m, 2H), 6.95 (d, J = 7.8 Hz, 1H), 6.89 (t, J = 7.3 Hz, 1H), 4.37 (s, 2H), 3.91 (s, 3H), 2.88 (dt, J = 10.3, 4.4 Hz, 4H), 1.62 (q, J = 2.9 Hz, 4H). MS (ESI+): 296.2 [M + H]$^+$.

Methyl 4-((1,3,4,5-tetrahydro-2H-benzo[c]azepin-2-yl)methyl) benzoate (***11d***). Light yellow solid; Yield: 61.5%.1H NMR (500 MHz, chloroform-*d*) δ 7.98 (t, J = 6.1 Hz, 2H), 7.36 (t, J = 6.3 Hz, 2H), 7.15 (d, J = 4.9 Hz, 2H), 7.08 (q, J = 6.3 Hz, 1H), 6.88 (t, J = 6.0 Hz, 1H), 3.91 (s, 3H), 3.85 (s, 2H), 3.57−3.54 (m, 2H), 3.15−3.32 (m, 2H), 2.93−2.90 (m, 2H), 1.77−1.74 (m, 2H). MS (ESI+): 296.2 [M + H]$^+$.

Methyl 4-((1,2,4,5-tetrahydro-3H-benzo[d]azepin-3-yl)methyl) benzoate (***11e***). Light yellow solid; Yield: 64.9%. ^{1}H NMR (500 MHz, chloroform-*d*) δ 8.04−7.97 (m, 2H), 7.50−7.44 (m, 2H), 7.14−7.07 (m, 3H), 6.97 (d, J = 7.2 Hz, 1H), 3.91 (d, J = 1.3 Hz, 3H), 3.73 (s, 2H), 3.63 (s, 2H), 2.90 (t, J = 6.0 Hz, 2H), 2.75 (t, J = 6.0 Hz, 2H). MS (ESI+): 296.2 [M + H]$^+$.

Methyl 4-((3,4,5,6-tetrahydrobenzo[c]azocin-2(1H)-yl)methyl) benzoate (***11f***). Light yellow solid; Yield: 66.5%. ^{1}H NMR (500 MHz, chloroform-*d*) δ 7.98 (d, J = 8.0 Hz, 2H), 7.53 (d, J = 7.9 Hz, 2H), 7.22 (td, J = 7.7, 1.7 Hz, 2H), 7.17−7.13 (m, 1H), 7.07 (td, J = 7.4, 7.0, 1.9 Hz, 1H), 4.20 (s, 2H), 3.89 (s, 3H), 3.01−2.82 (m, 2H), 2.71 (t, J = 5.9 Hz, 2H), 1.69 (t, J = 5.9 Hz, 2H), 1.64−1.54 (m, 2H), 1.22−1.18 (m, 2H). MS (ESI+): 310.2 $[M + H]^+$.

Methyl 4-((1,4,5,6-tetrahydrobenzo[d]azocin-3(2H)-yl)methyl) benzoate (***11g***). Light yellow solid; Yield: 70.1%. ^{1}H NMR (500 MHz, chloroform-*d*) δ 7.77 (q, J = 7.6 Hz, 4H), 7.22−7.17 (m, 3H), 7.11 (t, J = 6.3, 1H), 4.42−4.38 (m, 2H), 3.85 (s, 3H), 3.45−3.41 (m, 2H), 3.26−3.22 (m, 4H), 2.45−2.41 (m, 2H), 1.99−1.95 (m, 2H). MS (ESI+): 310.2 $[M + H]^+$.

Methyl 4-((1,3,4,5,6,7-hexahydro-2H-benzo[c]azonin-2-yl) methyl)benzoate (***11h***). Light yellow solid; Yield: 71.1%. ^{1}H NMR (500 MHz, chloroform-*d*) δ 7.75−7.65 (m, 2H), 7.35 (d, J = 7.8 Hz, 2H), 7.14 (t, J = 6.9 Hz, 1H), 7.07 (d, J = 7.6 Hz, 1H), 7.05−7.01 (m, 2H), 3.86 (s, 3H), 3.70−3.66 (m, 4H), 2.92−2.88 (m, 2H), 1.75−1.70 (m, 2H), 1.27−1.19 (m, 4H). MS (ESI+): 324.2 $[M + H]^+$.

Methyl 4-((octahydroquinolin-1(2H)-yl)methyl)benzoate (***11i***). Light yellow solid; Yield: 64.7%. 1H NMR (500 MHz, chloroform-*d*) δ 8.00−7.90 (m, 2H), 7.37 (d, J = 8.0 Hz, 2H), 4.10 (d, J = 14.1 Hz, 1H), 3.89 (s, 3H), 3.21 (d, J = 14.0 Hz, 1H), 2.79−2.72 (m, 1H), 2.16 (dt, J = 13.3, 3.6 Hz, 1H), 1.95 (td, J = 11.3, 3.5 Hz, 1H), 1.82−1.70 (m, 2H), 1.66−1.49 (m, 5H), 1.29−1.15 (m, 3H), 1.13−11.1 (m, 1H), 1.03−0.97 (m, 2H). MS (ESI+): 288.2 $[M + H]^+$.

Methyl 3-methoxy-4-((*2,3,4,5-tetrahydro-1H-benzo*[*b*]*azepin-1-yl*)*methyl*)*benzoate* (***14a***). Light yellow solid; Yield: 72.2%. ^{1}H NMR (500 MHz, chloroform-*d*) 7.58 (d, J = 7.7 Hz, 1H), 7.18−7.14 (m, 1H), 7.11−7.06 (m, 1H), 7.05 (td, J = 7.4, 1.5 Hz, 2H), 6.95 (d, J = 7.9 Hz, 1H), 6.74 (t, J = 7.2 Hz, 1H), 4.29 (s, 2H), 3.88 (s, 3H), 3.78 (s, 3H), 2.92−2.86 (m, 4H), 1.54−1.52 (m, 4H). MS (ESI+): 326.2 $[M + H]^+$.

Methyl 2-methoxy-4-((*2,3,4,5-tetrahydro-1H-benzo*[*b*]*azepin-1-yl*)*methyl*)*benzoate* (***14b***). Light yellow solid; Yield: 70.4%. ^{1}H NMR (500 MHz, chloroform-*d*) δ 7.43−7.36 (m, 2H), 7.27 (d, J = 7.8, 1H), 7.16 (dd, J = 7.4, 1.7 Hz, 1H), 6.96 (td, J = 7.6, 1.7 Hz, 1H), 6.94 (d, J = 8.0 Hz, 1H), 6.81−6.78 (m, 1H), 4.32 (s, 2H), 3.88 (s, 3H), 3.85 (s, 3H), 2.86 (m, 2H), 2.78−2.75 (m, 2H), 1.61−1.52 (m, 4H). MS (ESI+): 296.2 $[M + H]^+$.

Methyl 3-fluoro-4-((*2,3,4,5-tetrahydro-1H-benzo*[*b*]*azepin-1-yl*)*methyl*)*benzoate* (***14c***). Light yellow solid; Yield: 67.5%. ^{1}H NMR (500 MHz, chloroform-*d*) δ 7.45 (d, J = 7.9 Hz, 1H), 7.44 (d, J = 11.6 Hz, 1H), 7.34 (td, J = 7.8, 2.1 Hz, 1H), 7.17−7.10 (m, 2H), 6.96 (d, J = 7.8 Hz, 1H), 6.78−6.81 (m, 1H), 4.28 (s, 2H), 3.86 (s, 3H), 2.88−2.83 (m, 2H), 2.77−2.75 (m, 2H), 1.52 (q, J = 9.1, 7.2 Hz, 4H). MS (ESI+): 314.1 $[M + H]^+$.

Methyl 2-fluoro-4-((*2,3,4,5-tetrahydro-1H-benzo*[*b*]*azepin-1-yl*)*methyl*)*benzoate* (***14d***). Light yellow solid; Yield: 68.3%. ^{1}H NMR (500 MHz, chloroform-*d*) δ 7.48 (t, J = 7.6 Hz, 1H), 7.29−7.23 (m, 2H), 7.17−7.14 (m, 1H), 7.01 (s, 1H), 6.86 (d, J = 7.9 Hz, 1H), 6.79 (t, J = 7.3 Hz, 1H), 4.32 (s, 2H), 3.87 (s, 3H), 2.85−2.72 (m, 4H), 1.60−1.51 (m, 2H), 1.55−1.48 (m, 2H). MS (ESI+): 314.1 $[M + H]^+$.

5.2. *General procedure for synthesis of compounds* ***12a−i*** *and* ***15a−d***

To a stirred solution of solid NaOH (40 mg, 1.0 mmol) in 50% aqueous NH_2OH (0.8 mL) was added a solution of ester intermediates **11a−i** and **14a−d** (0.25 mmol) in THF/MeOH (1:1, 1.0 mL) dropwise at 0 °C. The resulting mixture was stirred for 30 min while warming to room temperature. The solution was neutralized with 2 mol/L HCl to pH ~7. The crude products were purified by a reverse phase C-18 column using Combiflash and lyophilized to give the desired compounds as white powder.

Methyl 4-((3,4-Dihydroquinolin-1(2H)-yl)methyl)-N-hydroxybenzamide (***12a***). Yield: 47.7%; ^{1}H NMR (500 MHz, DMSO-d_6) δ 7.68 (d, J = 8.0 Hz, 2H), 7.35 (d, J = 7.9 Hz, 2H), 7.14 (td, J = 7.1, 2.0 Hz, 1H), 7.09−7.04 (m, 1H), 7.02 (td, J = 7.5, 1.8 Hz, 2H), 3.69−3.65 (m, 4H), 2.90 (t, J = 6.3 Hz, 2H), 2.46−2.44 (m, 2H). ^{13}C NMR (126 MHz, DMSO-d_6) δ 163.4, 152.3, 143.5, 136.1, 131.6, 131.3, 128.4, 127.4, 127.0, 121.6, 118.2, 57.6, 54.5, 40.2 (2C), 35.8, 31.2. MS (ESI+): 283.2 $[M + H]^+$.

Methyl 4-((3,4-dihydroisoquinolin-2(1H)-yl)methyl)-N-hydroxybenzamide (***12b***). Yield: 40.5%. ^{1}H NMR (500 MHz, DMSO-d_6) δ 7.68 (d, J = 8.0 Hz, 2H), 7.38 (d, J = 7.9 Hz, 2H), 7.24 (td, J = 7.1, 2.0 Hz, 1H), 7.09−7.04 (m, 1H), 7.02 (td, J = 7.5, 1.8 Hz, 2H), 3.69−3.65 (m, 4H), 2.90 (t, J = 6.3 Hz, 2H), 2.46−2.44 (m, 2H). ^{13}C NMR (126 MHz, DMSO-d_6) δ 162.9, 151.5, 144.5, 136.2, 131.8, 130.7, 127.9, 127.3, 127.5, 121.5, 117.2, 56.5, 54.5, 41.2, 40.8, 35.5, 31.8. MS (ESI+): 283.2 $[M + H]^+$.

Methyl 4-((2,3,4,5-tetrahydro-1H-benzo[b]azepin-1-yl)methyl)-N-hydroxybenzamide (***12c***). Yield: 44.3%. ^{1}H NMR (500 MHz, DMSO-d_6) δ 11.12 (s, 1H), 8.97 (s, 1H), 7.66 (d, J = 7.7 Hz, 2H), 7.43 (d, J = 7.8 Hz, 2H), 7.06 (d, J = 7.3 Hz, 1H), 7.02 (t, J = 7.6 Hz, 1H), 6.90 (d, J = 7.9 Hz, 1H), 6.77 (t, J = 7.2 Hz, 1H), 4.31 (s, 2H), 2.79 (dt, J = 17.3, 4.8 Hz, 4H), 1.66−1.43 (m, 4H). ^{13}C NMR (126 MHz, DMSO-d_6) δ 164.7, 152.1, 143.6, 136.0, 131.9, 130.3, 128.4, 127.4, 127.0, 121.6, 118.1, 57.9, 54.5, 40.0 (2C), 34.9, 30.2, 25.9. MS (ESI+): 297.2 $[M + H]^+$.

Methyl 4-((1,3,4,5-tetrahydro-2H-benzo[c]azepin-2-yl)methyl)-N-hydroxybenzamide (***12d***). Yield: 41.2%. ^{1}H NMR (500 MHz, DMSO-d_6) δ 7.75−7.64 (m, 2H), 7.37 (d, J = 7.7 Hz, 2H), 7.20−7.09 (m, 3H), 7.03−7.69 (m, 1H), 3.74−3.68 (m, 2H), 3.30 (s, 1H), 2.87−2.76 (m, 2H), 2.51−2.43 (m, 1H), 2.38−2.32 (m, 2H), 1.64−1.52 (m, 2H), 1.52−1.39 (m, 2H). ^{13}C NMR (126 MHz, DMSO-d_6) δ 130.8, 130.0, 128.9, 128.0, 127.3, 126.3, 58.7, 54.0, 52.2, 40.0, 32.5, 30.9, 23.6. MS (ESI+): 297.2 $[M + H]^+$.

Methyl 4-((1,2,4,5-tetrahydro-3H-benzo[d]azepin-3-yl)methyl)-N-hydroxybenzamide (***12e***). Yield: 38.4%. ^{1}H NMR (500 MHz, DMSO-d_6) δ 11.56 (s, 1H), 11.43−11.16 (m, 1H), 7.83−7.74 (m, 2H), 7.69 (t, J = 6.3 Hz, 2H), 7.14 (d, J = 5.4 Hz, 4H), 4.37 (d, J = 5.6 Hz, 2H), 3.57−3.50 (m, 2H), 3.45−3.39 (m, 2H), 2.89 (dd, J = 33.6, 18.3, 9.4 Hz, 4H). ^{13}C NMR (126 MHz, DMSO-d_6) δ 139.8, 134.1, 132.2, 129.5, 127.65 (2C), 53.5, 40.0 (2C), 30.9. MS (ESI+): 297.2 $[M + H]^+$.

Methyl 4-((3,4,5,6-tetrahydrobenzo[c]azocin-2(1H)-yl)methyl)-N-hydroxybenzamide (***12f***). Yield: 66.5%; Purity: 98.2% (HPLC). ^{1}H NMR (500 MHz, DMSO-d_6) δ 7.73 (d, J = 7.8 Hz, 1H), 7.66 (d, J = 7.9 Hz, 1H), 7.27 (t, J = 7.7 Hz, 2H), 7.10 (d, J = 8.7 Hz, 2H), 7.03 (t, J = 7.5 Hz, 1H), 6.86 (d, J = 7.3 Hz, 1H), 4.22 (s, 2H), 2.97−2.92 (m, 2H), 2.84−2.81 (m, 2H), 2.19−2.15 (m, 2H), 1.62−1.58 (m, 4H). ^{13}C NMR (126 MHz, DMSO-d_6) δ 138.7, 138.2, 134.3, 133.7, 131.8, 131.2, 129.8, 128.7, 127.6 (2C), 60.7, 588, 51.4, 40.2 (2C), 29.9, 29.0, 28.7. MS (ESI+): 311.2 $[M + H]^+$.

Methyl 4-((1,4,5,6-tetrahydrobenzo[d]azocin-3(2H)-yl)methyl)-N-hydroxybenzamide (***12g***). Yield: 40.6%. ^{1}H NMR (500 MHz,

DMSO-d_6) δ 7.77 (q, J = 7.6 Hz, 4H), 7.19 (dd, J = 19.2, 7.3, 4.1 Hz, 3H), 7.10 (dt, J = 6.3, 3.2 Hz, 1H), 4.40 (dd, J = 13.1, 4.4 Hz, 1H), 4.25 (dt, J = 13.0, 5.4 Hz, 1H), 3.49 (dd, J = 25.7, 14.3, 9.0 Hz, 2H), 3.24 (td, J = 13.0, 12.6, 5.6 Hz, 1H), 3.11−2.90 (m, 3H), 2.49−2.43 (m, 1H), 2.37 (td, J = 13.4, 12.7, 5.5 Hz, 1H), 1.99−1.88 (m, 1H), 1.60−1.45 (m, 1H). ^{13}C NMR (126 MHz, DMSO-d_6) δ 139.2, 138.3, 134.1, 133.8, 131.9, 130.2, 129.6, 128.3, 127.6 (2C), 60.8, 58.7, 51.6, 40.0 (2C), 29.8, 29.0, 27.8. MS (ESI+): 311.2 $[M + H]^+$.

Methyl 4-((1,3,4,5,6,7-hexahydro-2H-benzo[c]azonin-2-yl)methyl)-N-hydroxybenzamide (***12h***). Yield: 38.8%. ^{1}H NMR (500 MHz, DMSO-d_6) δ 7.75−7.65 (m, 2H), 7.35 (d, J = 7.8 Hz, 2H), 7.14 (t, J = 6.9 Hz, 1H), 7.07 (d, J = 7.6 Hz, 1H), 7.05−7.01 (m, 2H), 3.70−3.66 (m, 4H), 2.92−2.88 (m, 2H), 1.75−1.70 (m, 2H), 1.27−1.19 (m, 4H). ^{13}C NMR (126 MHz, DMSO-d_6) δ 143.1 (2C), 130.3, 129.42, 127.8, 127.2, 125.9, 59.8, 58.8, 53.0, 40.0, 31.1, 27.6, 25.1. MS (ESI+): 325.2 $[M + H]^+$.

Methyl 4-((octahydroquinolin-1(2H)-yl)methyl)-N-hydroxybenzamide (***12i***). Yield: 40.9%. ^{1}H NMR (500 MHz, DMSO-d_6) δ 8.00−7.90 (m, 2H), 7.37 (d, J = 8.0 Hz, 2H), 4.10 (d, J = 14.1 Hz, 1H), 3.23−3.24 (m, 1H), 2.79−2.72 (m, 1H), 2.16 (dt, J = 13.3, 3.6 Hz, 1H), 1.96−1.92 (m, 1H), 1.82−1.70 (m, 2H), 1.66−1.49 (m, 5H), 1.29−1.15 (m, 3H), 1.13−11.1 (m, 1H), 1.03−0.97 (m, 2H). ^{13}C NMR (126 MHz, DMSO-d_6) δ 162.9, 146.2, 145.3, 136.6, 131.9, 130.7, 127.9, 77.3, 56.5, 54.5, 41.2, 40.8, 35.5, 32.5, 28.5, 25.8, 25.3. MS (ESI+): 289.2 $[M + H]^+$.

N-Hydroxy-3-methoxy-4-((2,3,4,5-tetrahydro-1H-benzo[b]azepin-1-yl)methyl)benzamide (***15a***). Yield: 45.2%. ^{1}H NMR (500 MHz, DMSO-d_6) δ 10.53 (s, 1H), 9.01 (s, 1H), 7.49 (d, J = 7.7 Hz, 1H), 7.13−7.10 (m, 1H), 7.09−7.05 (m, 1H), 7.02 (td, J = 7.4, 1.5 Hz, 2H), 6.92 (d, J = 7.9 Hz, 1H), 6.79 (t, J = 7.2 Hz, 1H), 4.29 (s, 2H), 3.78 (s, 3H), 2.82−2.76 (m, 4H), 1.56−1.53 (m, 4H). ^{13}C NMR (126 MHz, DMSO-d_6) δ 130.3 (2C), 127.1, 121.7, 120.3, 118.1, 111.5, 58.0, 56.0, 54.4, 40.0 (2C), 35.02, 30.4, 26.0. MS (ESI+): 327.2 $[M + H]^+$.

N-Hydroxy 2-methoxy-4-((2,3,4,5-tetrahydro-1H-benzo[b]azepin-1-yl)methyl)benzamide (***15b***). Yield: 36.6%. ^{1}H NMR (500 MHz, DMSO-d_6) δ 11.13 (s, 1H), 8.97 (s, 1H), 7.33−7.30 (m, 2H), 7.25 (dd, J = 7.8, 1.5 Hz, 1H), 7.04 (dd, J = 7.4, 1.7 Hz, 1H), 6.97 (td, J = 7.6, 1.7 Hz, 1H), 6.77 (d, J = 8.0 Hz, 1H), 6.75−6.71 (m, 1H), 4.29 (s, 2H), 3.83 (s, 3H), 2.89 (m, 2H), 2.78−2.74 (m, 2H), 1.63−1.50 (m, 4H). ^{13}C NMR (126 MHz, DMSO-d_6) δ 164.5, 157.3, 135.2, 130.8, 130.4, 128.8, 127.0, 121.1, 119.3, 117.6, 109.6, 56.0, 54.4, 51.9, 40.0, 34.7, 29.8, 25.8. MS (ESI+): 297.2 $[M + H]^+$.

3-*Fluoro-N-hydroxy-4-((2,3,4,5-tetrahydro-1H-benzo[b]azepin-1-yl)methyl)benzamide* (***15c***, *PB118*). Yield: 47.5%. ^{1}H NMR (500 MHz, DMSO-d_6) δ 9.36 (s, 1H), 7.47 (d, J = 7.9 Hz, 1H), 7.40 (d, J = 11.6 Hz, 1H), 7.33 (td, J = 7.8, 2.1 Hz, 1H), 7.07−7.00 (m, 2H), 6.91 (d, J = 7.8 Hz, 1H), 6.77 (td, J = 7.4, 2.1 Hz, 1H), 4.29 (d, J = 2.2 Hz, 2H), 2.87−2.80 (m, 2H), 2.77−2.70 (m, 2H), 1.51 (q, J = 9.1, 7.2 Hz, 4H). ^{13}C NMR (126 MHz, DMSO-d_6) δ 152.1, 135.9, 130.3, 130.0, 127.1, 122.1, 121.5, 117.9, 112.9 (2C), 54.1, 51.1, 40.0, 34.7, 30.0, 25.8. MS (ESI+): 315.2 $[M + H]^+$. ^{19}F NMR (282 MHz, DMSO-d_6): δ −119.6 (s, 1F). HRMS (ESI): exact mass calcd for $C_{18}H_{19}FN_2O_2$ [M+ H^+], 315.1531; found, 315.15046.

2-*Fluoro-N-hydroxy-4-((2,3,4,5-tetrahydro-1H-benzo[b]azepin-1-yl)methyl)benzamide* (***15d***). Yield: 48.3%. ^{1}H NMR (500 MHz, DMSO-d_6) δ 10.90 (s, 1H), 9.25 (s, 1H), 7.46 (t, J = 7.6 Hz, 1H), 7.29−7.20 (m, 2H), 7.07 (dd, J = 7.3, 1.7 Hz, 1H), 7.02 (td, J = 7.7, 1.7 Hz, 1H), 6.89 (d, J = 7.9 Hz, 1H), 6.78 (t, J = 7.3 Hz, 1H), 4.33 (s, 2H), 2.86−2.73 (m, 4H), 1.62−1.54 (m, 2H), 1.54−1.47 (m, 2H). ^{19}F NMR (282 MHz, DMSO-d_6): δ −113.9 (s, 1F). ^{13}C NMR (126 MHz, DMSO-d_6) δ 130.3, 127.1, 124.3, 121.8, 118.1, 115.7 (2C), 57.4, 54.7, 40.0 (2C), 34.8, 30.2, 25.9. MS (ESI+): 315.2 $[M + H]^+$.

5.3. LogD determination

The method of log*D* determination was described in our previous literature[44]. In brief, PB118 was dissolved in DMSO to a concentration of 10 mmol/L. Aliquots (15 μL) of the stock solution was mixed with 100 μL *n*-octanol in 1 mL PBS buffer (pH 7.4). The resulting mixture was shaken for 1 h in a rotator at 30 rpm at room temperature. The concentrations of PB118 in *n*-octanol and water were measured by LC−MS (Agilent 6310 ion trap mass spectrometer). Experiments were performed in duplicate. Then the log$D_{7.4}$ was calculated by log [the ratio between the amount of test compound in *n*-octanol and PBS].

5.4. Molecular docking study

The molecular docking study was performed as our previous procedures[38,45]. Briefly, The zHDAC6 crystal structure was obtained from Protein Data Bank (6 TH V, www.rcsb.org). The original ligand (Tubastatin A) and the water molecules were removed by PyMOL. PB118 was docked with the binding pocket in the enzyme using AutoDock Vina (v 1.1.2). The plots of protein−ligand interaction between PB118 and zHDAC6 were generated using PyMOL.

5.5. Radiosynthesis of [^{18}F]PB118

[^{18}F]fluoride ion was trapped in a QMA-light Sep-Pak cartridge (130 mg) which was pretreated with EtOH (10 mL), 1 mol/L K_2CO_3 (10 mL), and then sterile water (10 mL) to remove [^{18}O]water and the other possible impurities. Trapped [^{18}F]fluoride was eluted into the reaction vial containing a stir bar using 1.0 mL of acetonitrile/water solution (acetonitrile/water = 4/1, *v*/*v*) containing 13 mg kryptofix 222 and 3.5 mg of K_2CO_3. Then, the resulting solution was dried by azeotropic distillation under nitrogen (N_2) at 100 °C. After the solvent was dried, 1.0 mL anhydrous acetonitrile was added to the vial and repeated the dry down process twice. A solution of the borate precursor (**16**, 0.02 mmol), $Cu(OTf)_2$ $(py)_4$ (0.03 mmol) in 500 μL DMA was added to the vial, and the mixture was stirred at 120 °C for 20 min. Then the vial was cooled to room temperature and quenched using 0.1% TFA in water (1.5 mL) and then purified by reverse-phase semipreparative HPLC (Column: Agilent Eclipse XDB-C18, 5 μm, 250 mm × 9.4 mm, flow rate = 5.0 mL/min, mobile phase = 0.1% TFA in water/0.1% TFA in acetonitrile, 29/71, *v*/*v*). The desired fraction ([^{18}F]**14c**, retention time = 11.2−12 min) was collected and then loaded onto a solid-phase exchange (SPE) C-18 cartridge, rinsed with H_2O (5 mL). The C-18 cartridge was eluted with 0.6 mol/L NaOH in MeOH/THF (1:1, 1.0 mL) into a vial containing 100 μL hydroxylamine aqueous solution (50% (*w*/*w*) in H_2O). After stirring at room temperature for 10 min, 1 mL of 3 mol/L HCl was added to the mixture. The resulting mixture was injected into a reverse-phase semipreparative HPLC for purification (Column: Agilent Eclipse XDB-C18, 5 μm, 250 mm × 9.4 mm, flow rate = 5.0 mL/min, mobile phase = 0.1% TFA in water/0.1% TFA in acetonitrile, 58/42, *v*/*v*). The desired

fraction ([^{18}F]PB118, retention time = 4.5−5 min) was collected. The average time required for the synthesis from the end of cyclotron bombardment to end of synthesis was approximate 90−120 min. The average radiochemical yield was 9.2%−11% (nondecay corrected to trapped [^{18}F]fluoride, $n = 6$). Chemical and radiochemical purities were ≥95% with a specific activity 110 GBq/μmol (EOB). For more analytical data, refer to Supporting Information Fig. S1.

5.6. HDAC1−11 enzyme inhibition assays

HDAC inhibition assay of target compounds was carried out at Nanosyn (Santa Clara, CA, USA). Test compounds were diluted in 100% DMSO using 3-fold dilution steps. The final compound concentration in the assay ranged from 10 μmol/L to 0.056 nmol/L. Compounds were tested in a single well for each dilution, and the final concentration of DMSO in all assays was kept at 1%. Reference compounds, TSA was tested in an identical manner.

5.7. PET/CT imaging in rodents

The PET/CT imaging studies in rodents in this work were referred to our previous work[46,47]. Micro-PET/CT imaging was performed in two groups: male C57BL/6 mice, used for general brain imaging and blocking studies; female 5xFAD transgenic mice and their age and gender-matched WT mice, used as AD model. After intravenous injection of [^{18}F]PB118 (3.7−5.6 Mbq per animal), a 60-min dynamic PET acquisition was performed and followed a 10-min CT scan. For the blocking experiments, mice were pretreated with unlabeled PB118 or tubastatin A 5 min before the radiotracer injection. PET data were reconstructed using a 3D-MLEM method resulting in full width at a half-maximum resolution of 1 mm. These files were imported and analyzed using PMOD (PMOD 4.01, PMOD Technologies Ltd., Zurich, Switzerland).

5.8. NHP PET/MR acquisition and post processing

Male rhesus macaques were deprived of food for 12 h prior to the imaging study for the PET/MR scanning. Anesthesia was induced with intramuscular xylazine (0.5−2.0 mg/kg) and ketamine (10 mg/kg). The macaques were antecubital catheterized for radiotracer injection and a radial arterial line was placed for plasma and metabolite analysis. After endotracheal intubation, V-line and A-line were inserted, and the anesthetic state was maintained using isoflurane (∼1.5%) throughout the imaging studies. PET/MR images of the brain were acquired on a 3T Siemens TIM-Trio with a BrainPET insert (Siemens, Munich, Germany) and custom 8-channel head coil with an isotropic PET resolution of 1.25 mm at isocenter. Dynamic PET image acquisition was initiated, followed by the administration of [^{18}F]PB118 (averaged dose: 5.07 mCi). A MEMPRAGE sequence was acquired 30 min after the start of the scan for anatomic co-registration. For the blocking experiments, macaque was pretreated with unlabeled PB118 (1.0 mg/kg) at 10 min before the radiotracer injection. Dynamic data from the PET scans were recorded in list mode and corrected for attenuation, scatter, and decay. Macaque data were reconstructed using a 3D-OSEM method into progressive longer time frames for data analysis. Reconstructed PET images were then converted to standard-update values (SUV) by dividing the injected dose and weight of the NHP.

5.9. NHP PET/MR image analysis

PET data were motion-corrected and registered to the INIA19 Template and NeuroMaps Atlas for brain imaging analysis. Image registration was carried out on a high-resolution MPRAGE MRI image using a twelve degree-of-freedom linear algorithm and a nonlinear algorithm to the atlas brain. The transformation was then applied to the simultaneously collected dynamic PET data. VOIs were selected according to the macaque brain atlas. TACs were exported from the whole brain, cerebellum, amygdala, hippocampus, thalamus, nucleus accumbens and motor cortex VOIs for analysis. For representative images, SUV data from 90 to 120 min were averaged and subsequently overlayed on the INIA19 NHP brain template.

5.10. Western blot analysis

Human brain tissues were obtained from NIH NeuroBioBank (see details in Table S2). The tissue lysates were obtained by homogenization in cold RIPA buffer (89900, Thermo Fisher) containing proteinase inhibitor (05892970001, Roche) and 8 mol/L urea with a PRO200 homogenizer. Supernatants were collected and total protein concentrations were measured by using a BCA Protein Assay Kit (23227, Thermo Scientific). Equal amounts of protein (25 μg) were used for electrophoresis on 4%−20% Criterion TGX stain-free precast gels (5678095, Bio-Rad) and electrophoretically transferred onto PVDF membranes (1620264, Millipore). The membranes were blocked in 5% fat-free 1 hoat room temperature and then probed with antibody against HDAC-6 (1:1000, 07−732, Millipore) and GAPDH (1:10,000, ab8245, Abcam) overnight at 4 °C. The blots were then incubated for 1 h with anti-rabbit (1:5000, #7074, Cell Signaling Technology) secondary antibodies at room temperature. Signal was visualized using ECL Solution and Imager (Bio-Rad). Densitometry of protein bands was analyzed by Image J. For the quantification of the protein, the band intensities were normalized by GAPDH as an internal reference. Subsequently, normalized band intensities were divided by the average of the control group to determine normalized fold change *vs*. the control groups.

5.11. Immunohistochemistry

We performed immunohistochemistry (IHC) staining following methods that have been previously reported[15,35,48]. In brief, we utilized both WT and 5xFAD (tg) mice brain sections ($n = 3$) which were washed four times with PBS (17-512F, Lonza) for 30 min. Then, to block the non-specific staining, brain sections were incubated in donkey serum solution [5% donkey serum (D9663, Sigma) with 0.3% Triton X-100 (TX1568-1, Merck) in PBS] for 1 h at room temperature in a shaker with gentle shaking. Then we carefully discarded the blocking buffer and added the anti-rabbit HDAC6 (1:200, #D21B10, Cell Signaling Technology) and anti-rat GFAP (1:500, #13-0300, Invitrogen) primary antibody mixture (prepared in 2.5% donkey serum with 0.3% Triton X-100 in PBS) and incubated overnight in the cold room with gentle shaking. Thereafter, brain sections were washed four times in PBS for 30 min and incubated in a secondary antibody mixture [1:500 dilution of Alexa-488 labeled anti-rat and 1:500 dilution of Alexa-594 tagged anti-rabbit IgG antibodies (Jackson ImmunoResearch Lab Inc.)] prepared in 2.5% donkey serum with 0.3% TritonX-100 in PBS) at room temperature for 2 h with gentle shaking. Then, sections were washed twice with PBS for 20 min and incubated in 2 nmol/L of Hoechst (33342, Thermo Scientific) in PBS for

10 min. Finally, brain sections were washed with PBS for 20 min, carefully mounted on Invitrogen Prolong Gold antifade reagent (P36934, Invitrogen) after draining PBS, covered with a coverslip, and imaged in a Nikon C2 confocal microscopy.

Acknowledgments

This research was supported by pilot funding from the Martinos Center (to Changning Wang, USA) and the Cure Alzheimer's Fund, USA.

Author contributions

All co-authors reviewed the paper and provided comments. Changning Wang, Rudolph E. Tanzi, Can Zhang, Se Hoon Choi provided supervision. Changning Wang, Rudolph E. Tanzi, Can Zhang, Se Hoon Choi, Hsiao-Ying Wey, and Ping Bai designed the experiments and interpreted the results. Changning Wang, Can Zhang, Frederick A. Bagdasarian, Nisha Rani and Ping Bai analyzed the data. Ping Bai, Prasenjit Mondal, Yan Liu, Ashley Gomm, Darcy R. Tocci, Frederick A. Bagdasarian, Nisha Rani, Hsiao-Ying Wey carried out the experiments. Ping Bai primarily wrote the manuscript.

Conflicts of interest

The authors declare no conflict of interest.

Appendix A. Supporting information

Supporting data to this article can be found online at https://doi.org/10.1016/j.apsb.2022.05.017.

References

1. Bird A. Perceptions of epigenetics. *Nature* 2007;**447**:396−8.
2. de Ruijter AJ, van Gennip AH, Caron HN, Kemp S, van Kuilenburg AB. Histone deacetylases (HDACs): characterization of the classical HDAC family. *Biochem J* 2003;**370**(Pt 3):737−49.
3. Witt O, Deubzer HE, Milde T, Oehme I. HDAC family: what are the cancer relevant targets?. *Cancer Lett* 2009;**277**:8−21.
4. Hubbert C, Guardiola A, Shao R, Kawaguchi Y, Ito A, Nixon A, et al. HDAC6 is a microtubule-associated deacetylase. *Nature* 2002;**417**:455−8.
5. Simões-Pires C, Zwick V, Nurisso A, Schenker E, Carrupt PA, Cuendet M. HDAC6 as a target for neurodegenerative diseases: what makes it different from the other HDACs?. *Mol Neurodegener* 2013;**8**:1−16.
6. Aldana-Masangkay GI, Sakamoto KM. The role of HDAC6 in cancer. *J Biomed Biotechnol* 2011;**2011**:875824.
7. Dallavalle S, Pisano C, Zunino F. Development and therapeutic impact of HDAC6-selective inhibitors. *Biochem Pharmacol* 2012;**84**:756−65.
8. Pulya S, Amin SA, Adhikari N, Biswas S, Jha T, Ghosh B. HDAC6 as privileged target in drug discovery: a perspective. *Pharmacol Res* 2021;**163**:105274.
9. Huang P, Almeciga-Pinto I, Jarpe M, van Duzer JH, Mazitschek R, Yang M, et al. Selective HDAC inhibition by ACY-241 enhances the activity of paclitaxel in solid tumor models. *Oncotarget* 2017;**8**:2694−707.
10. Santo L, Hideshima T, Kung AL, Tseng JC, Tamang D, Yang M, et al. Preclinical activity, pharmacodynamic, and pharmacokinetic properties of a selective HDAC6 inhibitor, ACY-1215, in combination with bortezomib in multiple myeloma. *Blood* 2012;**119**:2579−89.
11. Cook C, Gendron TF, Scheffel K, Carlomagno Y, Dunmore J, DeTure M, et al. Loss of HDAC6, a novel CHIP substrate, alleviates abnormal tau accumulation. *Hum Mol Genet* 2012;**21**:2936−45.
12. Dompierre JP, Godin JD, Charrin BC, Cordelieres FP, King SJ, Humbert S, et al. Histone deacetylase 6 inhibition compensates for the transport deficit in Huntington's disease by increasing tubulin acetylation. *J Neurosci* 2007;**27**:3571−83.
13. Fukada M, Hanai A, Nakayama A, Suzuki T, Miyata N, Rodriguiz RM, et al. Loss of deacetylation activity of HDAC6 affects emotional behavior in mice. *PLoS One* 2012;**7**:e30924.
14. Odagiri S, Tanji K, Mori F, Miki Y, Kakita A, Takahashi H, et al. Brain expression level and activity of HDAC6 protein in neurodegenerative dementia. *Biochem Biophys Res Commun* 2013;**430**:394−9.
15. Govindarajan N, Rao P, Burkhardt S, Sananbenesi F, Schluter OM, Bradke F, et al. Reducing HDAC6 ameliorates cognitive deficits in a mouse model for Alzheimer's disease. *EMBO Mol Med* 2013;**5**:52−63.
16. Trzeciakiewicz H, Ajit D, Tseng JH, Chen Y, Ajit A, Tabassum Z, et al. An HDAC6-dependent surveillance mechanism suppresses tau-mediated neurodegeneration and cognitive decline. *Nat Commun* 2020;**11**:5522.
17. Ding H, Dolan PJ, Johnson GV. Histone deacetylase 6 interacts with the microtubule-associated protein tau. *J Neurochem* 2008;**106**:2119−30.
18. Kim C, Choi H, Jung ES, Lee W, Oh S, Jeon NL, et al. HDAC6 inhibitor blocks amyloid beta-induced impairment of mitochondrial transport in hippocampal neurons. *PLoS One* 2012;**7**:e42983.
19. Cheng KC, Hwang YL, Chiang HC. The double-edged sword effect of HDAC6 in Aβ toxicities. *FASEB J* 2022;**36**:e22072.
20. Li Y, Sang S, Ren W, Pei Y, Bian Y, Chen Y, et al. Inhibition of histone deacetylase 6 (HDAC6) as a therapeutic strategy for Alzheimer's disease: a review (2010−2020). *Eur J Med Chem* 2021;**226**:113874.
21. Choi H, Kim HJ, Yang J, Chae S, Lee W, Chung S, et al. Acetylation changes tau interactome to degrade tau in Alzheimer's disease animal and organoid models. *Aging Cell* 2020;**19**:e13081.
22. Fan SJ, Huang FI, Liou JP, Yang CR. The novel histone de acetylase 6 inhibitor, MPT0G211, ameliorates tau phosphorylation and cognitive deficits in an Alzheimer's disease model. *Cell Death Dis* 2018;**9**:1−14.
23. Majid T, Griffin D, Criss IIZ, Jarpe M, Pautler RG. Pharmocologic treatment with histone deacetylase 6 inhibitor (ACY-738) recovers Alzheimer's disease phenotype in amyloid precursor protein/presenilin 1 (APP/PS1) mice. *Alzheimers Dement* 2015;**1**:170−81.
24. Choi H, Kim HJ, Kim J, Kim S, Yang J, Lee W, et al. Increased acetylation of Peroxiredoxin 1 by HDAC6 inhibition leads to recovery of Abeta-induced impaired axonal transport. *Mol Neurodegener* 2017;**12**:1−14.
25. Ametamey SM, Honer M, Schubiger PA. Molecular imaging with PET. *Chem Rev* 2008;**108**:1501−16.
26. Tago T, Toyohara J. Advances in the development of PET ligands targeting histone deacetylases for the assessment of neurodegenerative diseases. *Molecules* 2018;**23**:300.
27. Wang C, Schroeder FA, Wey HY, Borra R, Wagner FF, Reis S, et al. *In vivo* imaging of histone deacetylases (HDACs) in the central nervous system and major peripheral organs. *J Med Chem* 2014;**57**:7999−8009.
28. Wey HY, Wang C, Schroeder FA, Logan J, Price JC, Hooker JM. Kinetic analysis and quantification of [11C] Martinostat for *in vivo* HDAC imaging of the brain. *ACS Chem Neurosci* 2015;**6**:708−15.
29. Strebl MG, Campbell AJ, Zhao WN, Schroeder FA, Riley MM, Chindavong PS, et al. HDAC6 brain mapping with [^{18}F] bavarostat enabled by a Ru-mediated deoxyfluorination. *ACS Cent Sci* 2017;**3**:1006−14.
30. Celen S, Rokka J, Gilbert TM, Koole M, Vermeulen I, Serdons K, et al. Translation of HDAC6 PET imaging using [(18)F]EKZ-001-cGMP production and measurement of HDAC6 target occupancy in nonhuman primates. *ACS Chem Neurosci* 2020;**11**:1093−101.

31. Koole M, Van Weehaeghe D, Serdons K, Herbots M, Cawthorne C, Celen S, et al. Clinical validation of the novel HDAC6 radiotracer [^{18}F] EKZ-001 in the human brain. *Eur J Nucl Med* 2021;**48**:596−611.
32. Wang XX, Wan RZ, Liu ZP. Recent advances in the discovery of potent and selective HDAC6 inhibitors. *Eur J Med Chem* 2018;**143**:1406−18.
33. Wang C, Schroeder FA, Hooker JM. Visualizing epigenetics: current advances and advantages in HDAC PET imaging techniques. *Neuroscience* 2014;**264**:186−97.
34. Kozikowski AP, Shen S, Pardo M, Tavares MT, Szarics D, Benoy V, et al. Brain penetrable histone deacetylase 6 inhibitor SW-100 ameliorates memory and learning impairments in a mouse model of fragile X syndrome. *ACS Chem Neurosci* 2018;**10**:1679−95.
35. Choi SH, Bylykbashi E, Chatila ZK, Lee SW, Pulli B, Clemenson GD, et al. Combined adult neurogenesis and BDNF mimic exercise effects on cognition in an Alzheimer's mouse model. *Science* 2018;**361**:6406.
36. Oakley H, Cole SL, Logan S, Maus E, Shao P, Craft J, et al. Intraneuronal beta-amyloid aggregates, neurodegeneration, and neuron loss in transgenic mice with five familial Alzheimer's disease mutations: potential factors in amyloid plaque formation. *J Neurosci* 2006;**26**:10129−40.
37. Shen S, Svoboda M, Zhang G, Cavasin MA, Motlova L, McKinsey TA, et al. Structural and *in vivo* characterization of Tubastatin A, a widely used histone deacetylase 6 inhibitor. *ACS Med Chem Lett* 2020;**11**:706−12.
38. Trott O, Olson A. AutoDock Vina: improving the speed and accuracy of docking with a new scoring function, efficient optimization, and multithreading. *J Comput Chem* 2010;**31**:455−61.
39. Strebl MG, Wang C, Schroeder FA, Placzek MS, Wey HY, Van de Bittner GC, et al. Development of a fluorinated class-I HDAC radiotracer reveals key chemical determinants of brain penetrance. *ACS Chem Neurosci* 2016;**7**:528−33.
40. Zhang L, Sheng S, Qin C. The role of HDAC6 in Alzheimer's disease. *J Alzheimers Dis* 2013;**33**:283−95.
41. Anderson KW, Chen J, Wang M, Mast N, Pikuleva IA, Turko IV. Quantification of histone deacetylase isoforms in human frontal cortex, human retina, and mouse brain. *PLoS One* 2015;**10**:e0126592.
42. Mahady L, Nadeem M, Malek-Ahmadi M, Chen K, Perez SE, Mufson EJ. Frontal cortex epigenetic dysregulation during the progression of Alzheimer's disease. *J Alzheimers Dis* 2018;**62**:115−31.
43. Sen A, Nelson TJ, Alkon DL. ApoE 4 and Abeta oligomers reduce BDNF expression *via* HDAC nuclear translocation. *J Neurosci* 2015;**35**:7538−51.
44. Bai P, Lu X, Liu Y, Lan Y, Wang H, Fiedler S, et al. Discovery of a positron emission tomography radiotracer selectively targeting the BD1 bromodomains of BET proteins. *ACS Med Chem Lett* 2021;**12**:282−7.
45. Bai P, Wang K, Zhang P, Shi J, Cheng X, Zhang Q, et al. Development of chalcone-*O*-alkylamine derivatives as multifunctional agents against Alzheimer's disease. *Eur J Med Chem* 2019;**183**:111737.
46. Bai P, Lan Y, Wang H, Liu Y, Striar R, Yuan G, et al. Synthesis and characterization of a positron emission tomography imaging probe selectively targeting the second bromodomain of bromodomain protein BRD4. *Bioconjugate Chem* 2021;**32**:1711−8.
47. Bai P, Lan Y, Patnaik D, Wang H, Liu Y, Chen Z, et al. Design, synthesis, and evaluation of thienodiazepine derivatives as positron emission tomography imaging probes for bromodomain and extra-terminal domain family proteins. *J Med Chem* 2021;**64**:14745−56.
48. Liang Y, Raven F, Ward JF, Zhen S, Zhang S, Sun H, et al. Upregulation of Alzheimer's disease Amyloid-beta protein precursor in astrocytes both *in vitro* and *in vivo*. *J Alzheimers Dis* 2020;**76**:1071−82.